PERGAMON

International Journal of Solids and Structures 39 (2002) 3555–3580

INTERNATIONAL JOURNAL OF SOLIDS and STRUCTURES

www.elsevier.com/locate/ijsolstr

Ring fragmentation predictions using the Gurson model with material stability conditions as failure criteria

R. Becker *

Lawrence Livermore National Laboratory, Livermore, CA 94551, USA

Received 2 August 2001; received in revised form 9 October 2001

Abstract

The Gurson constitutive model used in combination with failure criteria based on material stability and bifurcation has been used in a finite element model to predict fracture and fragmentation in a dynamic expanding ring experiment. Integration of the constitutive relation is through a two level iteration scheme operating only on scalar equations. It provides a robust solution for the large strain increments expected in shock problems. Numerically efficient failure criteria based on a bifurcation analysis and Drucker's condition for material stability are evaluated at each integration point and at every time step. The models were used to predict the fracture strain and number of fragments for thin, electromagnetically loaded, expanding rings. The results show good predictions of time to failure. Predictions of the number of fragments are generally good, with the model based on Drucker's hypothesis being better at the higher strain rates. © 2002 Elsevier Science Ltd. All rights reserved.

Keywords: Bifurcation; Failure; Fragmentation; Gurson; Material stability

1. Introduction

Fracture of ductile metals by the process of void nucleation, growth and coalescence is a common phenomenon that has received considerable attention over the years. While much progress has been made toward understanding ductile fracture, for various reasons, many concepts and models that have been developed remain under utilized. The goal of this work is to synthesize a few of these existing ideas and models into full scale simulations to demonstrate not only their utility but also the capability to predict complex behavior from relatively simple models.

The basis for the fracture simulations is the evolution of damage through void growth predicted by the Gurson (1977) constitutive relation. This model provides for the growth of porosity as a function of deformation and stress state and for the degradation of strength due to the presence of the porosity. The Gurson (1977) model has been analyzed extensively. While there are issues related to the inclusion of work

* Fax: +1-925-423-0455.
E-mail address: becker13@llnl.gov (R. Becker).

0020-7683/02/$ - see front matter
PII: S0020-7683(02)00170-1

hardening (Leblond et al., 1995), strain rate sensitivity (Liu et al., submitted) and initial and evolving anisotropy (Kailasam et al., 2000), it remains a popular model because it is relatively simple, is well understood, and gives reasonable results.

The damage evolution model is only one piece of the fracture model. Nucleation models describing the creation of voids and coalescence models capturing the fracture event are also needed. The void nucleation model by Chu and Needleman (1980) was chosen for use here because it is straightforward and has been used in numerous simulations. Various fracture criteria have been proposed for use with the Gurson model. Most depend on combinations of void fraction, void geometry and strain (e.g. Brown and Embury, 1973; Johnson and Addessio, 1988; Thomason, 1999; Pardoen and Hutchinson, 2000). A review of several models is given by Pardoen et al. (1998). Finite element analyses on void containing unit cells by Koplik and Needleman (1988) and Becker et al. (1988) suggest that such criteria can be useful, but the void fraction at coalescence is considerably less than might be expected based on geometric arguments alone.

The point of departure of the present work from most finite element calculations using the Gurson model is in the choice of failure criteria. Here, two rather old concepts for failure models are employed: material stability and bifurcation. The bifurcation model has been described nicely by Rice (1976) and was applied to the Gurson model for three-dimensional continuum calculations by Yamamoto (1978) and Saje et al. (1982). The model assumes a uniformly deforming body containing a planar band of the same material. Equilibrium and compatibility conditions are enforced across the band. The trivial solution is for the band to deform the same as the remainder of the material. The goal of the bifurcation analysis is to use the material stiffness tensor and determine if it is possible for the material in the band to deform differently from the remainder of the body while still satisfying compatibility and equilibrium conditions.

While conceptually straight forward, the bifurcation calculation requires that the band normal be specified. To use this model in a finite element code for a general stress history, one would need to sweep through a vast range of band angles in three dimensions for each integration point of the calculation. This is prohibitively expensive. Here, the computations are simplified by writing the material stiffness in the coordinate system of the principal stress. This drops many terms from the equations of the bifurcation condition. An assumption is then made that the band normal lies in the plane containing the largest and smallest principal stresses. This simplifies the bifurcation analysis to the point where it can be solved in closed form.

The second failure criterion examined is based on Drucker's (1959) hypothesis on material stability. It states that the product of the stress rate and the strain rate must be positive for a stable material. Here it is assumed that a material violating this condition will fail. There are objections to using this as a fracture criterion because there is no accounting for compatibility or continuing equilibrium. How the material in a specific volume would fail is not known. However, calculations of the deformation and fracture of small regions containing measured spatial distributions of porosity show complex deformation patterns (Becker, 1987). The fracture path in these regions is not planar nor is the deformation uniform along the fracture. Strain localization in these calculations roughly corresponds to a maximum true stress. A maximum true stress would coincide with loss of stability based on Drucker's criterion. While these results do not disprove the criticisms of using this as a fracture criterion, they do demonstrate that simple compatible configurations are not to be expected. The concept of basing failure on loss of material stability is worth exploring.

In the following, both the bifurcation condition (Rice, 1976) and Drucker's (1959) material instability criterion are applied to predict fragmentation of a magnetically driven expanding ring (Niordson, 1965; Gourdin et al., 1989; Olsen et al., in preparation). Evolution of damage in the ring is described by the Gurson (1977) model. A new robust implicit integration scheme for the constitutive relation is presented which provides accurate integration of the porosity for shock driven problems where strain increments can be large and the loading direction can change rapidly from one time step to the next. The algorithm differs from the implementations of Aravas (1987) and Mahnken (1999) in that it works on a nested set of scalar equations rather than tensor relations.

2. Model description

2.1. The modified Gurson yield function

The Gurson (1977) yield function has been modified by Tvergaard (1981) and Tvergaard and Needleman (1984). The modified form is written in terms of the von Mises effective stress, σ_e; the hydrostatic stress, σ_h; the average matrix material flow strength, $\bar{\sigma}$; and a bilinear function of the void volume fraction, f^*:

$$\phi = \frac{\sigma_e^2}{\bar{\sigma}^2} + 2q_1 f^* \cosh\left(\frac{3q_2\sigma_h}{2\bar{\sigma}}\right) - \left(1 + q_1^2 f^{*^2}\right), \tag{1}$$

where

$$\sigma_h = \frac{1}{3}\boldsymbol{\sigma} : \mathbf{I}; \quad \sigma_e = \sqrt{\frac{3}{2}\boldsymbol{\sigma}' : \boldsymbol{\sigma}'}; \quad \boldsymbol{\sigma}' = \boldsymbol{\sigma} - \sigma_h \mathbf{I}. \tag{2}$$

The constants q_1 and q_2 are fitting parameters added by Tvergaard (1981) to provide better agreement with results of detailed unit cell calculations. The void fraction modification, f^*, was introduced by Tvergaard and Needleman (1984). It is intended to simulate the rapid loss of strength accompanying void coalescence and is given by

$$f^* = \begin{cases} f & \text{if } f \leqslant f_c; \\ f_c + (f - f_c)\frac{f_u - f_c}{f_f - f_c} & \text{if } f > f_c. \end{cases} \tag{3}$$

The parameter f_c is the void fraction at which enhanced softening initiates, f_f is the void fraction at which the material is assumed to have lost all load carrying capacity, and $f_u = 1/q_1$ is the value of f^* which satisfies the yield function with zero stress.

2.2. Plastic strain rate

The rate of deformation tensor, $\mathbf{d}$, is decomposed additively into elastic and plastic parts

$$\mathbf{d} = \mathbf{d}^e + \mathbf{d}^p, \tag{4}$$

and it is further broken into volumetric and deviatoric components. Respectively, these are

$$d_v = \mathbf{d} : \mathbf{I} \qquad \text{and} \qquad \mathbf{d}' = \mathbf{d} - \frac{1}{3} d_v \mathbf{I}. \tag{5}$$

Assuming a normality flow rule, the plastic part of the rate of deformation tensor is specified in a direction normal to the yield surface as

$$\mathbf{d}^p = \lambda \frac{\partial \phi}{\partial \boldsymbol{\sigma}} = \lambda \left[\frac{3\boldsymbol{\sigma}'}{\bar{\sigma}^2} + f^* q_1 q_2 \frac{1}{\bar{\sigma}} \sinh\left(\frac{3q_2\sigma_h}{2\bar{\sigma}}\right)\mathbf{I}\right], \tag{6}$$

where λ is the plastic multiplier.

Equating the plastic dissipation rate of a representative volume element in tensor form with the plastic dissipation rate of average matrix properties results in

$$\bar{\sigma}\dot{\bar{\varepsilon}}(1 - f) = \boldsymbol{\sigma} : \mathbf{d}^p = \lambda \boldsymbol{\sigma} : \frac{\partial \phi}{\partial \boldsymbol{\sigma}} = 2\lambda \left[\frac{\sigma_e^2}{\bar{\sigma}^2} + \frac{3}{2} f^* q_1 q_2 \frac{\sigma_h}{\bar{\sigma}} \sinh\left(\frac{3q_2\sigma_h}{2\bar{\sigma}}\right)\right], \tag{7}$$

where $\dot{\bar{\varepsilon}}$ is an average effective plastic strain rate in the matrix material. A dimensionless parameter, $\bar{\lambda}$, is introduced to simplify the notation.

$$\bar{\lambda} = (1-f)\left[\frac{\sigma_e^2}{\bar{\sigma}^2} + \frac{3}{2} f^* q_1 q_2 \frac{\sigma_h}{\bar{\sigma}} \sinh\left(\frac{3 q_2 \sigma_h}{2\bar{\sigma}}\right)\right]^{-1}. \tag{8}$$

Using $\bar{\lambda}$ to solve Eq. (7) for λ, and substituting λ into Eq. (6), the plastic part of the rate of deformation tensor can be written as

$$\mathbf{d}^p = \dot{\bar{\varepsilon}}\bar{\lambda}\left[\frac{3}{2}\frac{\boldsymbol{\sigma}'}{\bar{\sigma}} + \frac{1}{2} f^* q_1 q_2 \mathbf{I} \sinh\left(\frac{3 q_2 \sigma_h}{2\bar{\sigma}}\right)\right]. \tag{9}$$

Eq. (9) is similar to Eq. (6) except that the matrix plastic strain rate appears explicitly and the term in brackets is dimensionless. The plastic strain rate is trivially decomposed into deviatoric and hydrostatic parts which facilitates development of the integration algorithm. In the integration scheme described below, the product $\dot{\bar{\varepsilon}}\bar{\lambda}$ is treated as the primary variable in the iterative solution of the equations.

For the strength relations in which $\dot{\bar{\varepsilon}}$ alone is needed, $\bar{\sigma}(\bar{\varepsilon}, \dot{\bar{\varepsilon}}, T, \ldots)$, it is obtained by dividing the current value of $\dot{\bar{\varepsilon}}\bar{\lambda}$ by the value of $\bar{\lambda}$ evaluated at the beginning of the time increment. $\bar{\lambda}$ is a slowly varying function of void fraction over a wide range of triaxialities (Fig. 1) and $\dot{\bar{\varepsilon}}$ is an approximate average value for the matrix strain rate in a representative volume element. It is felt that additional errors introduced to $\dot{\bar{\varepsilon}}$ in this operation will be relatively small compared to the approximations inherent in constructing an average matrix strain rate for a heterogeneous microstructure (Leblond et al., 1995; Liu et al., submitted).

2.3. Deviatoric relations

Assuming that the elastic behavior is isotropic and that the shear modulus, μ, depends on temperature and pressure, the deviatoric part of the Jaumann rate of Cauchy stress can be written

$$\overset{\nabla}{\boldsymbol{\sigma}}' = \frac{\dot{\mu}}{\mu}\boldsymbol{\sigma}' + 2\mu\mathbf{d}^{e'}. \tag{10}$$

Using an additive decomposition of the rate of deformation tensor into elastic and plastic parts and using $\mathbf{d}^{p'}$ from Eq. (9), the deviatoric part of the stress rate becomes

$$\overset{\nabla}{\boldsymbol{\sigma}}' = \frac{\dot{\mu}}{\mu}\boldsymbol{\sigma}' + 2\mu\mathbf{d}' - 3\mu\dot{\bar{\varepsilon}}\bar{\lambda}\frac{\boldsymbol{\sigma}'}{\bar{\sigma}}. \tag{11}$$

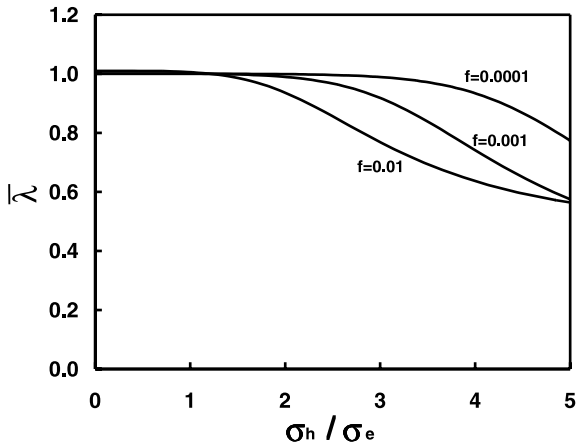

Fig. 1. Variation in dimensionless parameter $\bar{\lambda}$ as a function of triaxiality and void fraction.

Assuming that the applied strain rate and effective plastic strain rate are constant over a time increment, the deviatoric part of the stress tensor at the end of the time increment can then be written as

$$\boldsymbol{\sigma}' = \boldsymbol{\sigma}'_t + \frac{\Delta\mu}{\mu}\boldsymbol{\sigma}'_t + 2\mu\mathbf{d}'\,\Delta t - 3\mu\dot{\bar{\varepsilon}}\bar{\lambda}\,\Delta t\frac{\boldsymbol{\sigma}'}{\bar{\sigma}}, \tag{12}$$

where $\boldsymbol{\sigma}'_t$ has already been acted upon by the rigid body rotation increment to satisfy objectivity. In addition, the shear modulus and the increment in shear modulus appearing in the second and third terms on the right hand side are determined from conditions at the beginning of the time step. This is not necessary, but is simplifies the implementation considerably.

Combining the first three terms on the right hand side of Eq. (12) into a "trial stress", $\boldsymbol{\sigma}^T$, and moving the last term to the left hand side of the equation, the stress at the end of the time step is related to the trial stress by:

$$\boldsymbol{\sigma}'\left(1 + 3\mu\dot{\bar{\varepsilon}}\bar{\lambda}\,\Delta t/\bar{\sigma}\right) = \boldsymbol{\sigma}^T. \tag{13}$$

The inner product of this equation with itself and weighted by $3/2$ leads to

$$\frac{\sigma_{\mathrm{e}}}{\bar{\sigma}} = \frac{\sigma_{\mathrm{e}}^T}{\bar{\sigma} + 3\mu\dot{\bar{\varepsilon}}\bar{\lambda}\,\Delta t} \quad \text{with} \quad \sigma_{\mathrm{e}}^T = \sqrt{\frac{3}{2}\boldsymbol{\sigma}^T : \boldsymbol{\sigma}^T}. \tag{14}$$

These relations are similar to those utilized in J2-Flow theory.

Once σ_{e} is known, a combination of Eqs. (13) and (14) gives a straight forward means of calculating the deviatoric stress tensor in terms of the trial functions

$$\boldsymbol{\sigma}' = \frac{\sigma_{\mathrm{e}}}{\sigma_{\mathrm{e}}^T}\boldsymbol{\sigma}^T. \tag{15}$$

This is equivalent to the radial return strategy for J2-flow theory (Krieg and Krieg, 1977).

To facilitate evaluation of the yield function, Eq. (1), the stress ratio in the left hand side of Eq. (14) is substituted into the yield function. This replaces the equivalent stress with a simple function of the trial stress and the plastic strain rate. The substitution effectively eliminates σ_{e} from the yield function evaluation and replaces it with a function of the quantity $\dot{\bar{\varepsilon}}\bar{\lambda}$, which will be treated as the primary variable when iterating to satisfy the yield function.

2.4. Void growth and pressure relations

From Eq. (9), the rate of plastic volume change is given by

$$d_v^{\mathrm{p}} = \mathbf{d}^{\mathrm{p}} : \mathbf{I} = \frac{3}{2}\dot{\bar{\varepsilon}}\bar{\lambda}f^* q_1 q_2 \sinh\left(\frac{3q_2\sigma_{\mathrm{h}}}{2\bar{\sigma}}\right) = \dot{\bar{\varepsilon}}\bar{\lambda}f^* Z, \tag{16}$$

where Z has been introduced for convenience. The plastic volume change affects the evolution of both the hydrostatic stress and the void fraction. Hence, the evolution of σ_{h} and f are coupled through the dependence implicitly indicated in Eq. (16).

The evolution rate of the void fraction due to growth of existing voids is a function of the plastic volume change and is given by (Gurson, 1977)

$$\dot{f} = (1-f)d_v^{\mathrm{p}} = (1-f)\dot{\bar{\varepsilon}}\bar{\lambda}f^* Z. \tag{17}$$

The void fraction can also increase due to void nucleation by cracking of second phase particles or debonding of the matrix material from particles. The nucleated voids will grow subsequent to nucleation, but there is no plastic volume change associated with these nucleation events. Here, for simplicity, it is assumed

that growth of newly nucleated voids is negligible in the time step in which the nucleation event occurred. Newly nucleated voids affect the yield function, Eq. (1), but not the void growth relations for that time step. Since nucleation of new voids from second phase particles is assumed to not impact void growth in the same time increment, the nucleation models can be decoupled from void growth. The nucleation models will be discussed later.

Eq. (17) can be rewritten to look more like an ODE in f.

$$\frac{\mathrm{d}f}{(1-f)f^*} = \frac{\mathrm{d}f}{(1-f)(bf+a)} = \dot{\bar{\varepsilon}}\bar{\lambda}Z\,\mathrm{d}t, \tag{18}$$

where

$$a = \begin{cases} 0 & \text{if } f \leqslant f_c; \\ -f_c\frac{f_u - f_c}{f_f - f_c} & \text{if } f > f_c; \end{cases} \qquad b = \begin{cases} 1 & \text{if } f \leqslant f_c; \\ \frac{f_u - f_c}{f_f - f_c} & \text{if } f > f_c. \end{cases}$$

Eq. (18) can be integrated in closed form for f over the time step under the assumption that Z and the product $\dot{\bar{\varepsilon}}\bar{\lambda}$ are constant over the time increment. For the semi-implicit approach adopted here, $\dot{\bar{\varepsilon}}\bar{\lambda}$ is the average over the time increment and $Z = (Z_t + Z_{t+\Delta t})/2$ is the average of the function value from the beginning and end of the time increment. The expression for f at the end of the time increment is then

$$f = \frac{c-a}{c+b}; \qquad c = \frac{bf_t + a}{1-f_t}\exp\left[(a+b)\dot{\bar{\varepsilon}}\bar{\lambda}Z\,\Delta t\right], \tag{19}$$

where f_t is the void fraction at the beginning of the time increment.

This closed form integration is an important factor for the robustness of the model. The void fraction is well behaved and bounded ($0 \leqslant f \leqslant 1$) even though $\dot{\bar{\varepsilon}}\bar{\lambda}$ and Z can vary greatly in the iterative solution scheme. The integration of f in Eq. (19) is approximate in that σ_{h} is embedded in Z, and the hydrostatic stress does vary as a function of the void volume fraction over a time increment. The midpoint value of Z is used to improve accuracy.

To couple the plastic volume change to the pressure, it is assumed that the relative volume, $\overline{V}$, can be decomposed multiplicatively into portions due to elastic stretching, $\overline{V}^{\mathrm{e}}$ and void growth, $\overline{V}^{\mathrm{p}}$.

$$\overline{V} = \frac{V}{V_0} = \frac{V}{V^{\mathrm{p}}}\frac{V^{\mathrm{p}}}{V_0} = \overline{V}^{\mathrm{e}}\overline{V}^{\mathrm{p}}. \tag{20}$$

Here, V is the current volume, and V_0 is the stress free initial volume, including any initial voids. V^{p} represents the volume in an unstressed configuration affected only by growth of voids. Volume ratios are indicated by over-bars. $\overline{V}$ is provided by the finite element code for a displacement based formulation.

When voids are nucleated from particles, there is an increase in void fraction as it relates to the yield function. However, the nucleated void fraction, f_n, does not involve a volume change. Hence, when relating the void fraction (which includes both nucleation from particles and void growth) to the plastic volume change, the fraction of nucleated voids must removed. The void nucleating particles still occupy volume. Taking this and the initial void fraction, f_0, into account, the plastic component of the relative volume can be written in terms of void fraction as:

$$\overline{V}^{\mathrm{p}} = \frac{1-f_0}{1-(f-f_n)}. \tag{21}$$

The elastic component of the relative volume is used to determine the hydrostatic stress. Use of volume ratios or density ratios in equation of state (EOS) relations to determine pressure is common practice in the shock physics community. The formulation being developed here is intended to be compatible with these established relations. To illustrate a connection to more traditional solid mechanics notation, it is noted that $\overline{V}^{\mathrm{e}} = \exp(\varepsilon_v^{\mathrm{e}})$, where $\varepsilon_v^{\mathrm{e}}$ is the logarithmic elastic volume strain.

If it is assumed that a small porosity has a negligible effect on the elastic compressibility (compared to the plastic compressibility), the elastic component of the relative volume can be used directly in established EOS relations to calculate pressure.

$$-\sigma_{\mathrm{h}} = p = \mathscr{P}(\overline{V}^{\mathrm{e}}, T) = \mathscr{P}(\overline{V}\,\overline{V}^{\mathrm{p}-1}, T). \tag{22}$$

The temperature, T, is used to account for thermal expansion and temperature dependence of the elastic compressibility. This pressure–volume function, coupled with Eqs. (19)–(21), leads to an implicit equation for the hydrostatic stress with $\dot{\bar{\varepsilon}}\dot{\bar{\lambda}}$ as a parameter.

$$\psi = \sigma_{\mathrm{h}} + \mathscr{P}\left(\overline{V}, f(\sigma_{\mathrm{ht}}, \sigma_{\mathrm{h}}, \dot{\bar{\varepsilon}}\dot{\bar{\lambda}}, f_t), f_n, f_0, T\right) = 0. \tag{23}$$

For a given $\dot{\bar{\varepsilon}}\dot{\bar{\lambda}}$, Eq. (23) can be solved iteratively for σ_{h}. A combined bisection/Newton–Rhapson technique, such as described in Numerical Recipes (Press et al., 1992), ensures that a solution will be found as long as the interval containing the solution can be specified through bounds on the hydrostatic stress. Derivatives of ψ with respect to σ_{h} needed for the Newton–Rhapson iteration of Eq. (23) are given in Appendix A. The solution converges quadratically within the Newton–Rhapson portion of the algorithm.

2.5. Void nucleation from particles

Voids can nucleate from decohesion of the matrix material from particles or by particle cracking. The load which had been carried by the particles is relieved so that the yield function is affected by the nucleation event in the time step in which the nucleation event occurred. This loss of strength is simulated by an increase in the void fraction. Here, it is assumed that the growth of this newly nucleated void fraction is negligible over the current time increment, so the increment in void fraction due to nucleation is not coupled to the void growth described in Section 2.4. The growth of the newly nucleated voids will be treated in subsequent time steps. In the numerical algorithm this is accomplished by evaluating the void nucleation relations after the evaluation of the growth relations.

Void nucleation functions can take on many forms and are not difficult to incorporate under the given assumptions. The two nucleation models implemented in the current model were suggested by Chu and Needleman (1980). One provides for voids which nucleate due to strain incompatibility between the particles and the matrix. This could include particle fracture. The second is based on hydrostatic stress and is intended to capture decohesion or particle fracture due to a high tensile stress at the interface or within a particle.

The forms for both models are similar, so only the strain nucleation model is described. Voids are assumed to nucleate over a range of strains/stresses. The nucleation rate is assumed to follow a Gaussian distribution centered about some mean nucleation strain/stress. At low strains/stresses there is no nucleation. At higher values, the nucleation rate increases. The rate decreases beyond a certain strain/stress as most of the particles which could have nucleated voids have already done so.

The equation for the void nucleation rate is given by (Chu and Needleman, 1980)

$$\dot{f}_{\mathrm{N}\varepsilon} = \frac{f_{T\varepsilon}}{\varepsilon_{\mathrm{S}}\sqrt{2\pi}} \exp\left[-\frac{1}{2}\left(\frac{\bar{\varepsilon} - \varepsilon_{\mathrm{M}}}{\varepsilon_{\mathrm{S}}}\right)^2\right]. \tag{24}$$

Parameters for the strain nucleation model are:

(a) the volume fraction of voids to be nucleated, $f_{T\varepsilon}$;
(b) the mean value about which nucleation occurs, ε_{M};
(c) the standard deviation, ε_{S}; and
(d) a variable to track the level of nucleation which has already occurred, ε_{N}.

To avoid integration errors associated with potentially large changes in strain or hydrostatic stress over a time increment, Eq. (24) is not integrated numerically. Rather the distribution is integrated analytically as an error function, and the increment in void fraction nucleated over a time step is computed from the difference between two error functions:

$$\Delta f_{\mathrm{N}} = \frac{1}{2} f_{T_\varepsilon} \left[\operatorname{erf}\left(\frac{\bar{\varepsilon} + \dot{\bar{\varepsilon}} \Delta t - \varepsilon_{\mathrm{M}}}{\varepsilon_{\mathrm{S}} \sqrt{2}} \right) - \operatorname{erf}\left(\frac{\varepsilon_{\mathrm{N}} - \varepsilon_{\mathrm{M}}}{\varepsilon_{\mathrm{S}} \sqrt{2}} \right) \right]. \tag{25}$$

A similar set of equations is constructed for stress nucleation where the variable is the hydrostatic stress σ_{h}.

The increments in void fraction due to strain and stress nucleation are added to the void fraction computed from the growth relation, Eq. (19), using the hydrostatic stress computed from Eq. (23). Note that the void growth and the plastic strain rate or hydrostatic stress used to determine the void nucleation are functions of $\dot{\bar{\varepsilon}}\bar{\lambda}$.

2.6. Satisfying the yield function

The stress, plastic strain and void fraction at the end of a time increment are determined using a two level iteration scheme. For the inner iteration loop, the quantity $\dot{\bar{\varepsilon}}\bar{\lambda}$ is provided, and Eq. (23) is solved to give the hydrostatic stress and void fraction, as described in Section 2.4.

The outer iteration loop uses $\dot{\bar{\varepsilon}}\bar{\lambda}$ as the solution variable to satisfy the yield function, Eq. (1). The quantity $\sigma_{\mathrm{e}}/\bar{\sigma}$ from Eq. (14) and σ_{h} and f from the solution of Eq. (23) are substituted into Eq. (1). The matrix flow strength is determined from $\dot{\bar{\varepsilon}}\bar{\lambda}$ using the value of $\bar{\lambda}$ calculated at the beginning of the time increment. With these substitutions, Eq. (1) is a function of only $\dot{\bar{\varepsilon}}\bar{\lambda}$ for a given applied strain increment.

The value of $\dot{\bar{\varepsilon}}\bar{\lambda}$ satisfying the yield function is found using a combined bisection and Newton–Rhapson iteration scheme which ensures that the root will be found if it exists and can be bounded. The derivative of the yield function, ϕ, needed for the Newton–Rhapson iteration involves derivatives of Eq. (14) as well as quantities obtained from a linearization of Eq. (23) to account for the dependence of the hydrostatic stress and void fraction on $\dot{\bar{\varepsilon}}\bar{\lambda}$. These details are provided in Appendix B. The solution converges quadratically within the Newton–Rhapson portion of the algorithm.

The constitutive model was implemented in the finite element code ALE3D (Dube et al., 2001) which satisfies the dynamic stress equilibrium equations through either explicit time integration or backward difference implicit integration with Newton–Rhapson iteration on the global equilibrium equations.

The stability and convergence of the material integration algorithm are illustrated in Fig. 2. The calculations are of uniform tension and compression in a uniaxial strain mode which mimics the deformation state in shock loading. In this state, the axial strain is equal to volume strain. For simplicity, the matrix material is modeled as power law strain hardening with pressure independent elastic properties. The elastic shear modulus is 72 GPa, the bulk modulus 60 GPa, the yield stress 100 MPa and the hardening exponent 0.1. In tension the initial void fraction is 0.0001 and in compression it is 0.05. Loading to 5% volume strain is prescribed in 1, 10 or 1000 equal sized time increments.

The results in Fig. 2a show the void fraction and Fig. 2b shows the stress triaxiality, defined as $\sigma_{\mathrm{h}}/\sigma_{\mathrm{e}}$. Tension and compression are displayed on the same plot. The plots indicate that both the void fraction and the triaxiality are captured reasonably well with 10 time increments. For the calculations covering the 5% deformation in one time increment, the void fraction at the end of time step is in absolute error by less than 0.1% void fraction in tension and by much less in compression. There is a greater error in the tension calculation than in compression because of the non-linearities and path dependence associated with the high triaxiality needed to initiate plastic flow at the low initial volume fraction.

Since the void fraction is coupled directly to the prescribed volume change and pressure (through the elastic compressibility), the error in the void fraction can be traced to the over prediction of pressure at the

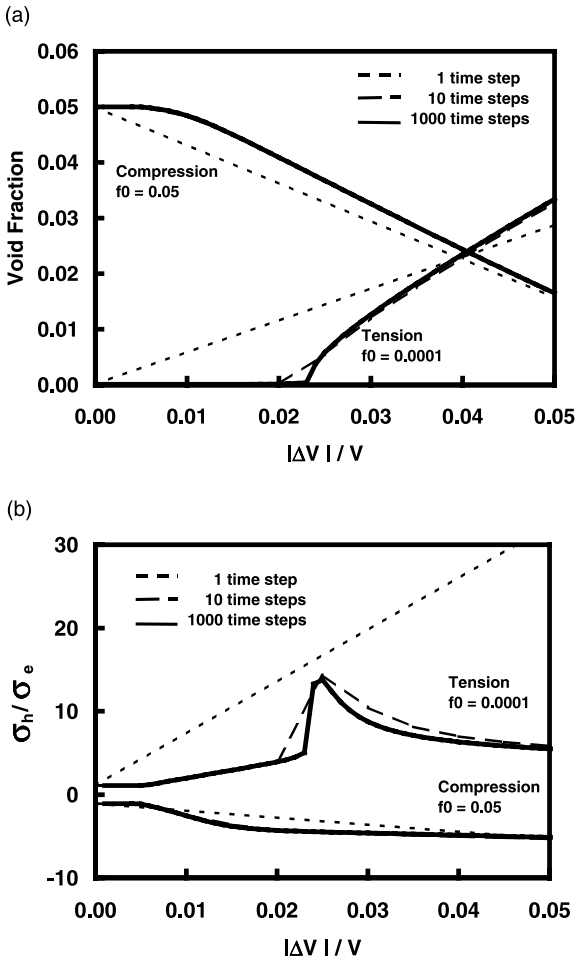

Fig. 2. Evolution of (a) void fraction and (b) stress triaxiality as a function of volume strain in uniaxial strain simulations to illustrate the solution dependence on time step size.

end of the time increment, Fig. 2b. The high pressure is necessary to offset the zero pressure at the beginning of the time increment in the central difference value of Z used in Eq. (19). Since the error in the void fraction shown in Fig. 2a is due to elastic strain, it will be corrected as the pressure returns to normal on successive time increments. A full backward difference scheme in Z was tried in hopes that it would give better pressures at the end of an increment. However, this resulted in significantly greater error in the estimation of the plastic strain rate ($\dot{\bar{\varepsilon}}\bar{\lambda}$) in larger calculations where the stress state flipped from plastically deforming in tension to plastically deforming in compression in one time increment.

2.7. Tangent stiffness

The tangent stiffness can be determined by a method that makes use of quantities already computed during the iterative solution to satisfy yield function. The starting point is the additive decomposition

of the stress into deviatoric and hydrostatic parts, Eq. (2) (third relation), and making use of Eqs. (14) and (15).

$$\boldsymbol{\sigma} = \frac{\bar{\sigma}}{\bar{\sigma} + 3\mu\dot{\bar{\varepsilon}}\bar{\lambda}\,\Delta t}\boldsymbol{\sigma}^T + \sigma_{\mathrm{h}}\mathbf{I}. \tag{26}$$

The tangent modulus for the incremental method is obtained by linearizing the stress increment with respect to the applied strain increment. Since the stress at the beginning of the time step is fixed, this is the same as linearizing the updated stress with respect to the strain increment.

After considerable manipulation (detailed in Appendix C) the tangent stiffness can be written as

$$\frac{\mathrm{d}\Delta\boldsymbol{\sigma}}{\mathrm{d}\Delta\boldsymbol{\varepsilon}} = A\mathscr{I}' + B\left(\frac{\boldsymbol{\sigma}'}{\bar{\sigma}} \otimes \frac{\boldsymbol{\sigma}'}{\bar{\sigma}}\right) + C\left(\frac{\boldsymbol{\sigma}'}{\bar{\sigma}} \otimes \mathbf{I}\right) + D\left(\mathbf{I} \otimes \frac{\boldsymbol{\sigma}'}{\bar{\sigma}}\right) + E(\mathbf{I} \otimes \mathbf{I}), \tag{27}$$

where the functions A, B, C, D and E are given in Appendix C and $\mathscr{I}'$ is a fourth order tensor function which operates on second order tensors and yields the deviatoric part of the input tensor. Although these expressions appear complex, most of quantities have been computed or are easily determined in the iteration loops satisfying Eq. (23) and the yield function. The additional computational cost is small.

3. Failure criteria

A failure criterion in the form of a critical void fraction has been included in the constitutive formulation (Eq. (3)). Failure criteria based on combinations of void fraction, strain, pressure and void size and spacing have also been proposed (e.g. Brown and Embury, 1973; Johnson et al., 1988; Thomason, 1999 and Pardoen and Hutchinson, 2000). An alternative approach is to utilize criteria for material stability and bifurcations which look for hints of failure susceptibility in the material response.

3.1. Simple material stability criterion

Failure might be viewed as the response of a material that has become unstable. Early work by Drucker (1959, 1960) suggests that a stable material can be characterized by the condition

$$\dot{\boldsymbol{\sigma}} : \dot{\boldsymbol{\varepsilon}} > 0 \tag{28}$$

and violation of this condition would indicate that the material is unstable. While generally used as a validity check when constructing yield surface models, this relation has been used by Drucker and Li (1993) as a failure criterion. Given the simple form of the criterion and availability of the stress and strain rate, it is easy to include this as a failure condition for each element of an analysis code. It adds little computational expense. This criterion will be investigated as one of several failure criteria.

In physical terms, the criterion suggests failure in uniaxial tension when the true stress reaches a maximum. This corresponds to the softening due to void growth exceeding the strain hardening rate.

3.2. Numerically tractable bifurcation model

A more widely applied failure criteria is a bifurcation condition where a material element is probed for a non-unique solution. In order to develop a tractable means of ascertaining a bifurcation condition, Yamamoto (1978) constructed a failure model following the bifurcation analysis of Rice (1976). The model assumes a homogeneously deforming body containing a planar slice of material in which the deformation may possibly localize. This model provides realistic fracture strain predictions which depend on the material properties and the stress state.

This bifurcation approach can be applied, in theory, to each integration point of a finite element analysis. However, a proper analysis requires searching for the orientation of the potential localization

band. This is not feasible, especially in the context of an explicit finite element code where the additional calculations could increase the computational time by at least an order of magnitude. Here, a simplified approach is adopted where approximations lead to a computationally tractable model. For completeness, a derivation of the model will be presented below. It is similar to the developments given by Yamamoto (1978) and Saje et al. (1982).

Consider a homogeneously deforming block of material in which a planar band, with normal $\mathbf{n}$, is defined, Fig. 3. At some point in the strain history it may be possible that the deformation in the band region could be different than the deformation in the surrounding material while still satisfying compatibility and equilibrium conditions. This is a bifurcation from the uniform state.

Compatibility conditions are constructed by assuming that the velocity gradient in the band, $\nabla \mathbf{V}_b$, is equal to the velocity gradient outside of the band, $\nabla \mathbf{V}_o$, plus a term depending on the band normal

$$\nabla \mathbf{V}_b = \nabla \mathbf{V}_o + \mathbf{g} \otimes \mathbf{n}. \tag{29}$$

The parameter $\mathbf{g}$ embodies the magnitude and direction of the velocity difference across the band. Traction equilibrium across the band requires that the tractions in the plane of the band be continuous across the interface

$$\mathbf{n} \cdot \boldsymbol{\sigma}_b = \mathbf{n} \cdot \boldsymbol{\sigma}_o. \tag{30}$$

In rate form this relation becomes

$$\mathbf{n} \cdot \dot{\boldsymbol{\sigma}}_b - \mathbf{n} \cdot (\nabla \mathbf{V}_b) \cdot \boldsymbol{\sigma}_b = \mathbf{n} \cdot \dot{\boldsymbol{\sigma}}_o - \mathbf{n} \cdot (\nabla \mathbf{V}_o) \cdot \boldsymbol{\sigma}_o. \tag{31}$$

The stress rate in Eq. (31) can be written terms of the Jaumann stress rate as

$$\dot{\boldsymbol{\sigma}} = \overset{\nabla}{\boldsymbol{\sigma}} + \boldsymbol{\omega} \cdot \boldsymbol{\sigma} - \boldsymbol{\sigma} \cdot \boldsymbol{\omega} = \mathscr{M} : \mathbf{d} + \boldsymbol{\omega} \cdot \boldsymbol{\sigma} - \boldsymbol{\sigma} \cdot \boldsymbol{\omega}, \tag{32}$$

where $\mathscr{M}$ is the material tangent modulus in the rate formulation. It is equal to the tangent stiffness described in Section 2.7 in the limit of a vanishing time increment. The rate of deformation tensor, $\mathbf{d}$, and the spin, $\boldsymbol{\omega}$, are expressed as

$$\mathbf{d} = \tfrac{1}{2}\left[(\nabla \mathbf{V}) + (\nabla \mathbf{V})^T\right] \quad \text{and} \quad \boldsymbol{\omega} = \tfrac{1}{2}\left[(\nabla \mathbf{V}) - (\nabla \mathbf{V})^T\right]. \tag{33}$$

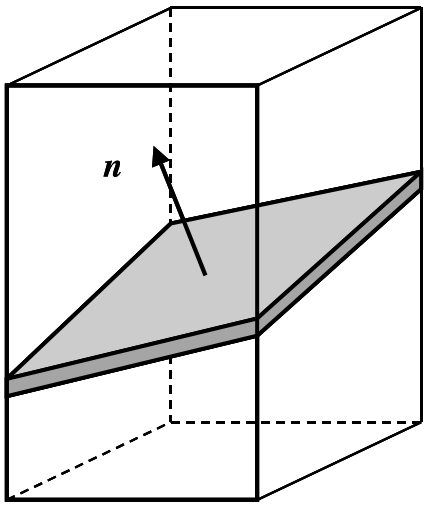

Fig. 3. Illustration of band configuration envisioned for bifurcation analysis.

Prior to bifurcation, the stress and tangent stiffness are uniform, and there is no distinction between values within and exterior to the band region. Using this condition and combining Eqs. (29) and (31)–(33), leads to

$$\mathbf{0} = \tfrac{1}{2}\mathbf{n}\cdot\mathscr{M} : [\mathbf{g}\otimes\mathbf{n} + \mathbf{n}\otimes\mathbf{g}] + \tfrac{1}{2}[\mathbf{n}\cdot(\mathbf{g}\otimes\mathbf{n})\cdot\boldsymbol{\sigma} - \mathbf{n}\cdot(\mathbf{n}\otimes\mathbf{g})\cdot\boldsymbol{\sigma} - \mathbf{n}\cdot\boldsymbol{\sigma}\cdot(\mathbf{g}\otimes\mathbf{n}) + \mathbf{n}\cdot\boldsymbol{\sigma}\cdot(\mathbf{n}\otimes\mathbf{g})] - \mathbf{n}\cdot(\mathbf{g}\otimes\mathbf{n})\cdot\boldsymbol{\sigma}. \tag{34}$$

Eq. (34) defines a system of linear equations in $\mathbf{g}$. Using Cartesian components of the tensors and vectors, the system of equations can be written

$$R_{ij}g_j = 0. \tag{35}$$

As long as R_{ij} is positive definite, the only solution is that $g_j = 0$, and the deformation continues to be uniform. When R_{ij} is no longer positive definite, or $\det[R_{ij}] \leqslant 0$, g_j can take on arbitrary values. This allows the possibility of strain localization within the band.

It is difficult to use Eq. (34) directly in a full scale numerical simulations since the band orientation must be specified. Searching for the band orientation is prohibitively expensive. However, one can take advantage of the form of the tangent modulus given in Eq. (27) to simplify the analysis. If the stress used in Eqs. (27) and (34) is in principal coordinates, the expressions simplify considerably. All of the cross coupling between the normal and shear components vanishes.

Using this idea, two solutions are constructed. One uses the actual calculated principal stresses and the other a fictitious set of principal stresses based on the current von Mises and hydrostatic stresses

$$\tilde{\sigma}_1 = \tfrac{1}{\sqrt{3}}\sigma_{\mathrm{e}} + \sigma_{\mathrm{h}} \quad \tilde{\sigma}_2 = -\tfrac{1}{\sqrt{3}}\sigma_{\mathrm{e}} + \sigma_{\mathrm{h}} \quad \tilde{\sigma}_3 = \sigma_{\mathrm{h}}. \tag{36}$$

These fictitious stresses are consistent with a plane strain stress state and they are of the same magnitude as the real stress in the material. The rational behind this second choice is that, over small regions, the local microstructure may produce stress states which are more favorable for strain localization. This is an attempt to explore the material response in such a stress state.

In both cases it will be assumed that the band normal has no component in the direction of the intermediate principal stress. For the case of the real principal stresses, possible configurations are omitted; and this will provide an upper bound for the bifurcation calculation. Since the stresses in the second solution are specified in a manner favorable for shear localization, this criterion will probably be met earlier in a general loading history. However, no comments can be made about this being any formal type of bound.

With the use of principal stresses and assuming the band normal lies in the plane of the largest and smallest principal stresses, the problem now resembles bifurcation in a planar tensile test. The bifurcation in a plane strain tension test was studied analytically by Hill and Hutchinson (1975), and some ideas that they developed can be employed.

With the given assumptions and using principal coordinates, the non-zero components of matrix for the bifurcation condition, Eq. (35), are given by:

$$\begin{aligned}
R_{11} &= [M_{1111} - \sigma_1]n_1^2 + [M_{1313} - \tfrac{1}{2}(\sigma_1' - \sigma_3')]n_3^2,\\
R_{13} &= [M_{1133} + M_{1313} - \tfrac{1}{2}(\sigma_1' + \sigma_3') - \sigma_{\mathrm{h}}]n_1 n_3,\\
R_{22} &= [M_{1212} - \tfrac{1}{2}(\sigma_2' - \sigma_1')]n_1^2 + [M_{2323} - \tfrac{1}{2}(\sigma_2' - \sigma_3')]n_3^2,\\
R_{31} &= [M_{3311} + M_{1313} - \tfrac{1}{2}(\sigma_3' + \sigma_1') - \sigma_{\mathrm{h}}]n_1 n_3,\\
R_{33} &= [M_{1313} - \tfrac{1}{2}(\sigma_3' - \sigma_1')]n_1^2 + [M_{3333} - \sigma_3]n_3^2.
\end{aligned} \tag{37}$$

This can be written in terms of the scalar coefficients of Eq. (27) as

$$
\begin{aligned}
R_{11} &= \left[\frac{2}{3}A + B\frac{\sigma'_1}{\bar{\sigma}}\frac{\sigma'_1}{\bar{\sigma}} + (C+D)\frac{\sigma'_1}{\bar{\sigma}} + E - \sigma'_1 - \sigma_h\right]n_1^2 + \left[\frac{1}{2}A - \frac{1}{2}(\sigma'_1 - \sigma'_3)\right]n_3^2,\\
R_{13} &= \left[\frac{1}{6}A + B\frac{\sigma'_1}{\bar{\sigma}}\frac{\sigma'_3}{\bar{\sigma}} + C\frac{\sigma'_1}{\bar{\sigma}} + D\frac{\sigma'_3}{\bar{\sigma}} + E - \frac{1}{2}(\sigma'_1 + \sigma'_3) - \sigma_h\right]n_1 n_3,\\
R_{22} &= \left[\frac{1}{2}A - \frac{1}{2}(\sigma'_2 - \sigma'_1)\right]n_1^2 + \left[\frac{1}{2}A - \frac{1}{2}(\sigma'_2 - \sigma'_1)\right]n_3^2,\\
R_{31} &= \left[\frac{1}{6}A + B\frac{\sigma'_3}{\bar{\sigma}}\frac{\sigma'_1}{\bar{\sigma}} + C\frac{\sigma'_3}{\bar{\sigma}} + D\frac{\sigma'_1}{\bar{\sigma}} + E - \frac{1}{2}(\sigma'_3 + \sigma'_1) - \sigma_h\right]n_1 n_3,\\
R_{33} &= \left[\frac{1}{2}A - \frac{1}{2}(\sigma'_3 - \sigma'_1)\right]n_1^2 + \left[\frac{2}{3}A + B\frac{\sigma'_1}{\bar{\sigma}}\frac{\sigma'_3}{\bar{\sigma}} + (C+D)\frac{\sigma'_3}{\bar{\sigma}} + E - \sigma'_3 - \sigma_h\right]n_3^2.
\end{aligned}
\tag{38}
$$

Following the ideas of Hill and Hutchinson (1975), the system of equations is divided by n_1 and the determinant set to zero. At this point, R_{22} is irrelevant for the analysis. The resulting equation is a quartic in the n_3/n_1. This ratio is the tangent of the band angle in the principal coordinate system. The quartic equation has only even powers so an analytic solution is possible. If there are no real roots for n_3/n_1 the equations are elliptic and there will be no bifurcation. If there are four real roots, the equations are hyperbolic and localization is possible. The existence of two real roots signifies parabolic relations, but based on the discussion by Hill and Hutchinson (1975), this condition is most likely inaccessible.

3.3. Behavior of the failure criteria

The failure criteria are investigated through calculations in several simple deformation states: uniaxial tension, plane strain tension and equi-biaxial tension. For these calculations the matrix strength relation is taken to be

$$\bar{\sigma}\ (\mathrm{MPa}) = 200 - 50\mathrm{e}^{-8\bar{\varepsilon}} \tag{39}$$

and the initial void fraction is 0.02. The applied nominal strain rate is 0.1 s^{-1} and the time step is limited to a maximum of 0.05 s to provide reasonable temporal resolution when picking the failure strains and void fractions from the tabulated results. Calculations are also run with the stress from Eq. (39) coupled in a power law strain rate sensitivity model with a reference strain rate of 0.1 s^{-1} and a rate sensitivity exponent of 0.002.

Results from these calculations are shown in Table 1. The columns labeled C_f indicate which of the three failure conditions became active first. The "D" indicates Drucker's (1959), the "B1" the bifurcation condition using the real principal stresses and "B2" the bifurcation condition using the contrived plane strain stress state. $\bar{\varepsilon}_{fail}$ is the failure strain, f_{fail} is the void fraction at failure and $h/\bar{\sigma}$ is the normalized hardening modulus at failure ($h \equiv \mathrm{d}\bar{\sigma}/\mathrm{d}\bar{\varepsilon}$). From Table 1 it is evident that the order of the failure strains is determined by the stress triaxiality. High triaxial stress states promote void growth and result in earlier failure.

Table 1
Predicted failure conditions for unit models

	Rate independent				Rate dependent			
	C_f	$\bar{\varepsilon}_{fail}$	f_{fail}	$h/\bar{\sigma}$	C_f	$\bar{\varepsilon}_{fail}$	f_{fail}	$h/\bar{\sigma}$
Uniaxial	B2	0.497	0.0262	0.0375	D	0.573	0.0268	0.0205
Plane strain	B1	0.407	0.0296	0.0776	D	0.479	0.0309	0.0434
Biaxial	B2	0.401	0.0312	0.0819	D	0.450	0.0324	0.0551

As might be expected, the bifurcation condition involving the real principal stresses triggers failure first in plane strain tension of the rate independent calculation. The bifurcation criterion has no approximations in this case. For the uniaxial tension and biaxial tension cases, the failure condition is reached earlier using the fictitious plane strain stress state. However, with just a bit more strain, failure based on Drucker's postulate would also be indicated in all three of the rate independent calculations.

It has been shown that even slight strain rate sensitivity will inhibit bifurcation (Hutchinson and Neale, 1978 and Needleman and Tvergaard, 1984). Consistent with this, none of the calculations with the rate dependent matrix material properties triggered a bifurcation even though the simulations are run to strains well in excess of those indicated in the rate independent analyses. However, all three of these simulations indicated failure based on a violation of Drucker's postulate. The strains and void fractions at failure for these rate dependent analyses are approximately the same as those of the rate independent calculations when Drucker's condition is first satisfied. Hence, the small rate sensitivity of the matrix material has only minor effects on failure predictions using this condition.

3.4. Computational cost of the model

The equations outlined in Section 2 are considerably more complex than J2-flow theory, and it is expected that the complexity would be reflected in computation time. One of the simulations described in the next section was run using both the void growth/failure model described above and a separate J2-flow theory implementation. Both use the same hardening model and EOS. The J2-flow theory model also solves for the plastic strain rate implicitly with the same iterative technique.

The calculation is explicit dynamic, so the evaluation of the constitutive model takes an appreciable fraction of the computation time for a J2-flow theory material. For this particular run, the calculation time was 5 times greater per time step with the void growth/failure model than it was for the J2-flow theory run.

4. Fragmentation predictions

Application of the constitutive model to high rate fracture simulations is demonstrated through a comparison to fragmentation results of expanding ring tests. Numbers of fragments and times to fracture are compared to experimental results. The sensitivity of the model to the numerical discretization and type and magnitude of the initial imperfection distribution is explored.

4.1. Description of ring experiments

An experiment used to evaluate material properties and fracture behavior of materials in the strain rate range of 10^3–10^4 s^{-1} is an electromagnetically driven expanding ring (Niordson, 1965). A schematic of the device used in these experiments is shown in Fig. 4 (Gourdin et al., 1989). A ring of material is placed concentrically over a mandrel containing a coil of wire. When current is applied to the wire, the magnetic field induced in the ring interacts with the applied magnetic field creating a uniform radial body force. If the force is large enough, the ring can deform plastically and increase its diameter. With yet higher forces, the ring expands rapidly and fractures dynamically.

By measuring the velocity of the ring and calculating the radial magnetic force, an energy balance can be used to determine the energy dissipated in the ring as it expands. Combining this with the strain and strain rate (also determined from the ring velocity), a stress–strain relation for uniaxial tension can be extracted for a relatively high strain rate. This procedure is simplified somewhat if the material has a low self inductance and magnetic forces driving the ring can be ignored. For such tests, a ring of the test material is

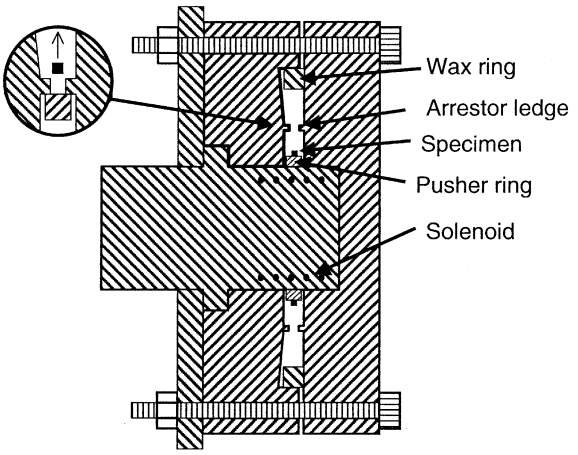

Fig. 4. Schematic of expanding ring experiment. (a) Loading device showing driving coils, test ring and wax capture ring; (b) configuration of test ring and drive ring for low conductivity materials.

placed over a ring of a material with a high conductance. This conductor not only drives the ring of test material, its conductance also shields the test ring from resistance heating. The drive ring has a greater thickness normal to the plane of the ring than the test material, Fig. 4. A mechanical stop is added to the fixture to arrest the driving ring at a given diameter. After the drive ring is stopped, the test ring will continue to expand driven by its radial inertia. As kinetic energy is dissipated by plastic deformation, the radial velocity of the ring decreases.

Experiments (Olsen et al., in preparation) were conducted on alloy rings of alloy U–6%Nb. The rings were initially 34.37 mm inside diameter, 35.89 mm outside diameter and 0.76 mm thick. The alloy develops little radial force when exposed to the magnetic field, so a drive ring of aluminum is fit to the inside diameter and used to propel the U–6%Nb ring. The stop for the drive ring is placed at a 20.0 mm radius. The drive ring is restrained at this point and the test ring continues to expand driven only by its radial inertia. The ring continues straining to fracture and the fragments are captured in wax at the outside of the test chamber.

The velocity of the ring is measured using laser interferometry. The test ring accelerates while in contact with the driving ring and begins to lose velocity as soon as the aluminum ring hits the stop. The radial kinetic energy is being converted to plastic strain energy. When the ring breaks, it is no longer dissipating energy and the recorded velocity becomes roughly constant. The unevenness of the fracture process introduces noise into the velocity trace.

The fragments are recovered and their number and size recorded. An example of the fractured ring and recovered aluminum drive ring are shown in Fig. 5. The dimpled fracture surface shown in the SEM micrograph in Fig. 6 confirms that fracture is dominated by ductile void growth and coalescence. Hence, the present models are relevant.

4.2. Ring fracture simulations

The ring fracture is simulated using the Gurson constitutive model with the three failure criteria described above. The calculations are run using the ALE3D (Dube et al., 2001) finite element code with explicit dynamic integration of the momentum equation. Fracture in an element is imposed by setting the stress to zero in elements as they reach the lowest of the failure criteria.

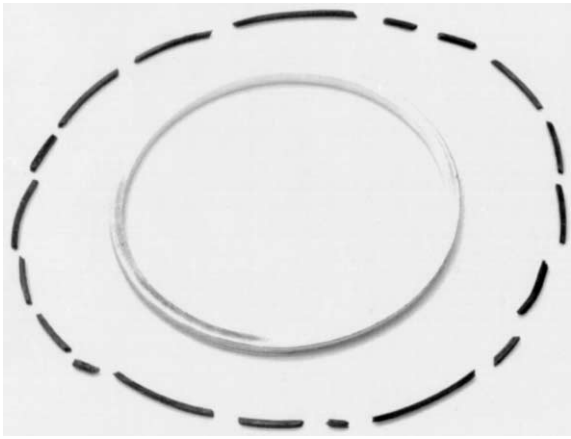

Fig. 5. Recovered fragmented test ring and arrested aluminum driver ring.

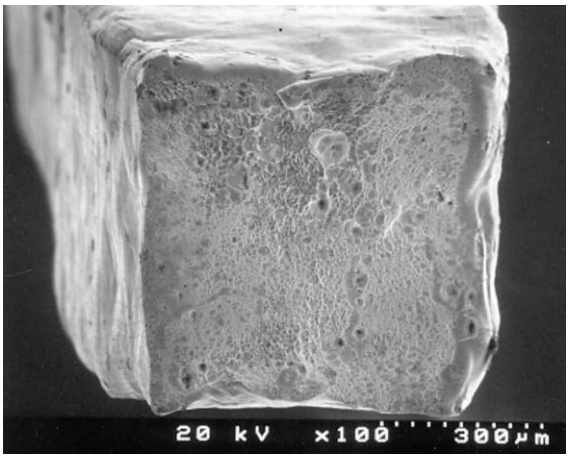

Fig. 6. SEM micrograph showing dimpled fracture surface characteristic of void related ductile failure.

The matrix material is specified to have a density of 17 300 kg/m^3, a constant bulk modulus of 80 GPa and a shear modulus of 72 GPa. The stress–strain behavior at a strain rate of 3000 s^{-1} was obtained from data collected by Cady et al. (1998) and is shown in Fig. 7. The sigmoidal shape is consistent with twinning being the primary deformation mechanism at low strains. This stress–strain relation is represented in the code in tabular form. One calculation is run with a strain rate sensitive material model. For this simulation the strain rate sensitivity exponent is specified as $m = 0.002$. Stress–strain data from separate constant rate tests show the curves converging at strains of approximately 0.2. This is where the data is important to the calculations. Strain rate jump tests are not available, so the best that can be done is to assume a small but finite value.

The alloy contains approximately 1.3% volume fraction of carbide particles which debond from the matrix or crack to form voids at low stresses (Sunwoo et al., submitted). In these calculations it will be assumed that an average 1.5% void fraction is present from the outset. From Mott's (1947) work it is known that a distribution of fragment sizes can be obtained by accounting for a spatial variation in fracture strain in the ring. Here this is achieved either through a random perturbation of the initial void fraction in

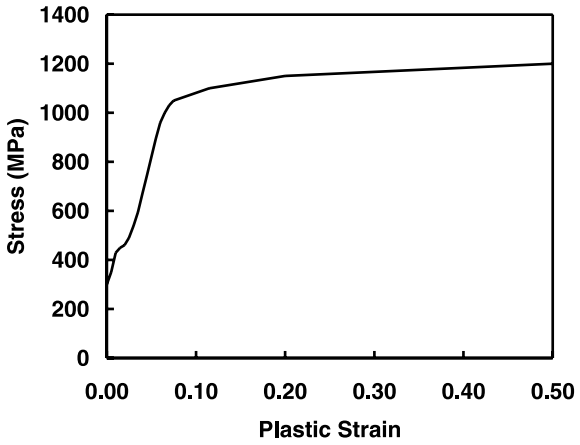

Fig. 7. Stress–plastic strain curve for U–6%Nb at a strain rate of 3000 s^{-1} and at 298 K (After Cady et al., 1998).

each element or through geometric defects. The void fraction distribution is created by using a random number generator to assign a perturbation from the mean value. The perturbations are uniformly distributed on either side of the mean value with specified perturbation maxima of 0.8%, 0.4% and 0.2%. The geometric imperfections are created by restricting the number of digits output by the mesh generator.

The finite element mesh used for the calculations is uniform and regular in the thickness, radial and circumferential directions. All non-uniformities in the solution are induced by the perturbations described above. For the majority of the calculations, the square cross-section of the ring is represented by a 5×5 mesh with 600 elements in the circumference. Mesh convergence calculations are performed by doubling the number of elements in each direction.

The full three-dimensional ring is modeled. Boundary conditions are initially imposed on the inside of the ring, consistent with the velocity of the driving the ring in the experiments. The velocity is specified to match the measured velocity up to the time when the drive ring hits the stop. At that time the boundary condition is removed and the ring continues to expand driven only by its radial inertia.

4.3. Results of ring simulations

Velocity–time plots for rings at three different accelerating voltages are shown in Fig. 8. The experimental results are indicated by the dark lines and the simulation results are shown by the shaded lines. For all cases in this figure, the initial imperfection is a 0.8% random perturbation in the void fraction and the mesh is $5 \times 5 \times 600$. Since the velocity in the simulations is prescribed initially, the agreement with the experiments up to the peak velocity is expected. Predictions begin after peak velocity.

Two features of the velocity curves are worthy of note. One is that the slope of the velocity decrease is captured by the simulation. This slope results from kinetic energy being dissipated as plastic deformation. Since the experimental and calculated velocities are the same, the agreement means that the flow strength is approximately correct. The second feature to notice is the point where the curves become noisier and the velocity becomes roughly constant. This indicates fracture. For the 7.5 and 6.0 kV driving voltages the model predicts fracture at roughly the right time. Since the velocities are also in close agreement, this means that fracture strains are captured reasonably well by the simulations. There were experimental difficulties with recording the velocity for the 5.0 kV test, so the experimental record is difficult to interpret.

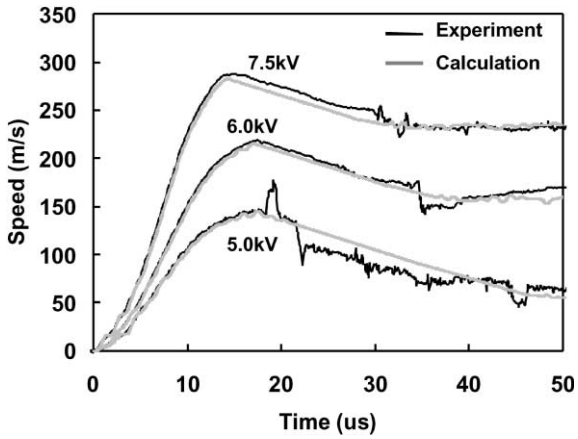

Fig. 8. Experimental and calculated velocity time history curves for rings at three accelerating voltages. The velocity was applied in the calculations from the beginning until peak velocity.

The predicted fragment pattern for a 7.5 kV driving force is shown in Fig. 9. While a statistical comparison has not been made, the fragment size distribution resembles that of the experiment shown in Fig. 5. There are also regions of the ring in which local necks have ceased deforming or where some elements have failed but fracture is arrested. These isolated failed elements are generally on the interior of the ring and are only seen in cross-sections. The arrest of localized necks and fractures is consistent with Mott's (1947) assumptions and the observations of Grady and Benson (1983). Simulations by Han and Tvergaard (1995), Sørensen and Freund (2000) and Pandolfi et al. (1999) also show arrested necks, although only the latter study predicts fracture and fragmentation.

As described by Mott (1947), the fragmentation behavior is governed by there being a distribution of fracture strain and the propagation of stress relief from newly created fracture sites. As the ring expands plastically, the stress and strain rate are initially uniform throughout the ring. At some point necking instabilities occur and many localized necks develop (Sørensen and Freund, 2000). These necks are at a much

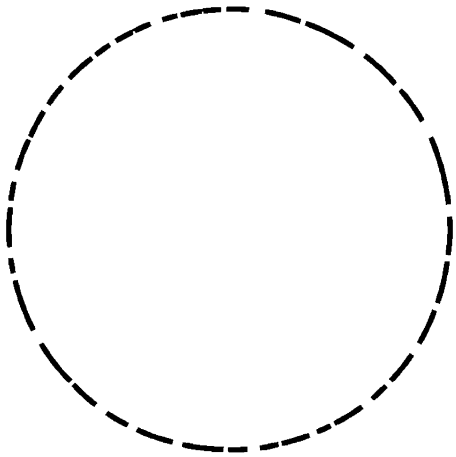

Fig. 9. Predicted ring fragmentation for 7.5 kV driving voltage, $5 \times 5 \times 600$ mesh and initial void fraction of 1.5% with a 0.8% perturbation.

closer spacing than the ultimate fracture sites. Due the distribution of porosity/damage, some of these necks will fail before others. When failure occurs at a location, a stress relief wave propagates from the fracture. If the stress relief reaches a neighboring neck prior to its fracturing, deformation is arrested. This propagating stress relief combined with the distribution of fracture strains sets the fragmentation pattern. For rings with higher strain rates, the relief wave cannot travel as far around the ring before neighboring necks reach their fracture strains. This leads to suppression of fewer fracture sites at higher strain rates and the creation of more fragments.

The sensitivity of the time to failure and number of fragments to imperfections, spatial discretization, strain rate sensitivity and fracture criterion are shown in Table 2. Experimental data from the 13 relevant tests are also included. The column labeled f_{pert} indicates the magnitude of the void fraction perturbation and the column *digits* is the number of significant digits of the nodal coordinates used to construct the finite element mesh. The time when failure is indicated by the calculated velocity trace going flat is in column t_f, and the number of fragments is in the column *frags*.

There is considerable scatter in the experimental data among duplicate tests, so the strains to failure are approximate and the number of fragments are given as a range. There were only three experiments run at the lower voltage, and none has a clean velocity trace from which to extract a time to failure.

Several things can be noticed from the results. First is that the model provides a reasonable prediction of the time to failure for all three accelerating voltages and with many types and magnitudes of imperfections. Second, the predicted number of fragments is in good agreement with experiments at the lowest voltage, and the calculations overestimate the number of fragments at higher strain rates. Third, the predicted time to failure and number of fragments is relatively insensitive to the changes in magnitude of the void fraction perturbation. The results are more sensitive to the geometric perturbations.

Table 2
Predicted ring failure conditions

Forc. (kV)	Mesh	f_{Pert} (%)	Digits	t_f (μs)	# Frags.
7.5	$5 \times 5 \times 600$	0.8	16	32	33
7.5	$5 \times 5 \times 600$	0.4	16	33	34
7.5	$5 \times 5 \times 600$	0.2	16	31	37
7.5	$10 \times 10 \times 1200$	0.8	16	31	37
7.5[a]	$5 \times 5 \times 600$	0.8	16	31	23
7.5[b]	$5 \times 5 \times 600$	0.8	16	25	18
7.5	$5 \times 5 \times 600$	0.0	16	55	60
7.5	$5 \times 5 \times 600$	0.0	7	43	43
7.5	$5 \times 5 \times 600$	0.0	4	34	24
7.5	Experiment			~30	21, 23,
7.5					26, 28
6.0	$5 \times 5 \times 600$	0.8	16	37	24
6.0	$5 \times 5 \times 600$	0.2	16	40	27
6.0	$10 \times 10 \times 1200$	0.8	16	36	28
6.0[a]	$5 \times 5 \times 600$	0.8	16	38	16
6.0	Experiment			~35	16, 18, 18,
6.0					19, 20, 20
5.0	$5 \times 5 \times 600$	0.8	16	46	12
5.0	$5 \times 5 \times 600$	0.2	16	51	8
5.0	$10 \times 10 \times 1200$	0.8	16	46	14
5.0[a]	$5 \times 5 \times 600$	0.8	16	50	9
5.0	Experiment			???	8, 11, 13

[a] Only failure based on Drucker's criteria active.
[b] Power law strain rate dependence with $m = 0.002$.

It is also significant that the predictions are relatively insensitive to the spatial resolution. This suggests that the dominant physical mechanisms are captured sufficiently by the coarser grid. The three most important aspects of the fragmentation are: the formation of multiple incipient necks; fracture within necked regions; and propagation of stress relief from a fracture. The first and third fall within the standard purview of finite element calculations, so it is no surprise that a reasonable mesh would capture these aspects. Mesh sensitivity might be expected for the fracture propagation at the cross-section level, but apparently the cross-section failure takes place so rapidly that it does not alter the timing of the relief waves enough to make an appreciable impact on the solution.

In all simulations using a rate independent material model and where all three failure criteria described in Section 3 are available, fracture occurs first for the bifurcation model with the fictitious plane strain stress state. Additional calculations were run in which only Drucker's (1959) criterion was available to predict fracture. A rather interesting result is how the choice of fracture criterion does not affect the time to failure significantly, but it does impact the number of fragments, particularly at the higher strain rates. In comparing the predictions with experiments, it appears that predictions based on Drucker's criterion are better. While this may be the case, a decisive conclusion about it being a more appropriate failure criterion should not be made based on this limited analysis.

A calculation was also run with the 7.5 kV driving force and a rate dependent material model. Since the chosen bifurcation models precluded failure for a rate dependent material, fracture is predicted by Drucker's criterion. Both the time at fracture and number of fragments are lower than for the rate independent analyses. The reason for this is not understood.

4.4. Fragmentation of a spherical shell

A demonstration calculation is also run predicting fragmentation of a spherical shell. For this calculation, 1/8 symmetry is assumed for a shell which is initially 3 mm thick and 100 mm inside radius. There are 600 000 eight-node brick elements used with five through the thickness of the shell. Loading is achieved

Fig. 10. Demonstration calculation illustrating the type of fracture pattern which can be predicted. 600 000 element mesh of hexahedral elements with five elements through the thickness.

by applying a 70 MPa internal pressure which was gradually ramped on over a 1 μs interval. This pressure is approximately four times the pressure to cause initial yield for the given geometry and material properties.

The resulting fragmentation pattern is shown in Fig. 10. Since this is only a toy problem with no experiments available for comparison, it only serves to illustrate the type of fragmentation patterns that can be predicted for more complex objects. It is not known if the fragmentation pattern or fragment size predictions are accurate.

Symmetry requires that all fractures intersect the symmetry planes at right angles. More intricate patterns with fine and coarse fractures are seen away from the boundaries. As with the rings, the fragment size is determined primarily by the propagation of stress relief from cracks which form earlier.

5. Discussion

An integration algorithm for the Gurson model has been presented which iterates on a nested pair of scalar equations to satisfy the yield function. The algorithm is robust and is able to provide reasonable stress and void fraction results for rather large strain increments and with large porosity changes. Such robust algorithms are necessary when the material is subjected to shock loading. Computation of the material stiffness is straight forward, and the algorithm will also work well for quasi-static analyses.

Failure criteria based on concepts of material stability and bifurcation have been implemented at the integration point level in a finite element code to simulate ductile fracture. With these criteria the failure predictions are naturally sensitive to the stress state, deformation history, strain hardening and evolving damage in the form of porosity predicted by the Gurson model. There is no need to prescribe failure conditions based on specific levels of void fraction, stress or strain. Although the situation did not arise here, creating fracture oblique to finite element grid lines can leave isolated elements bridging a fracture. In such cases an additional strain-based failure criterion would be useful to initiate failure in these elements.

Simulations of expanding ring experiments demonstrate that the failure models provide realistic predictions of strain to fracture and numbers of fragments using both geometric and material defects and over a wide range of perturbations. Since the creation of the fragment distribution is dominated by progression of stress relief from fracture locations, the predictions are relatively insensitive to spacial discretization as long as the there are several elements between fracture sites.

Further validation with other materials and deformation histories will be necessary for a thorough evaluation of the applicability of the failure criteria. From these results, fracture based on Drucker's hypothesis appears to give reasonable results for both rate independent and rate dependent materials. It is also easy and inexpensive to calculate.

The key feature provided by the fracture model for these fragmentation predictions is a reasonable distribution of fracture strains. Other models providing a distribution of failure strains would likely also produce realistic fragmentation. The advantage to using a microstructurally base model, such as the current one, is that the fracture strain and distribution predictions are related to observables in the microstructure and deformation conditions.

Although the ring experiments are dynamic, the strain rates are only on the order of 10^3–10^4 s^{-1}. This is several orders of magnitude lower than strain rates in a shock. Stress waves move across the specimen in a fraction of a microsecond. The strain increment across a 10 μm void is on the order of 10^{-5} per wave transit, and the stress waves offer only minor perturbations to the stress field around a void. Under such conditions, it would seem that the Gurson model should be as valid as it would be for quasi-static simulations.

This would not be the case for shock loaded porosity where imposed stress gradients are significant and wave reflections from voids important. For simulations involving shocks, it is anticipated that there may be appreciable error in damage prediction during the shock transit. However, if one is interested in

post-shock fracture response of an initially void free material, the Gurson model may provide reasonable predictions. One way to approach such a problem would be to use a strain induced void nucleation criterion where the nucleation strain is slightly above the strain that would accumulate from the initial shock plus that of a possible reflected shock from a free surface. This will prevent non-physical predictions of spall. Voids will then nucleate and grow with subsequent deformation. The current implementation facilitates this approach by providing a robust numerical scheme and using established EOS relations to treat shocks.

Acknowledgements

This work was performed under the auspices of the US Department of Energy by the University of California, Lawrence Livermore National Laboratory under Contract W-7405-Eng-48, UCRL-JC-144777.

Appendix A

The Newton–Rhapson iteration scheme applied to Eq. (23),

$$\psi = \sigma_{\mathrm{h}} + \mathscr{P}\left(\overline{V}, f(\sigma_{\mathrm{h}t}, \sigma_{\mathrm{h}}, \dot{\bar{\varepsilon}}\bar{\lambda}, f_t), f_n, f_0, T\right) = 0. \tag{A.1}$$

requires linearization of ψ in terms of σ_{h}, and determination of the correction to σ_{h} through

$$\psi_{n+1} \simeq 0 = \psi_n + \frac{\mathrm{d}\psi}{\mathrm{d}\sigma_{\mathrm{h}}}\,\delta\sigma_{\mathrm{h}}, \tag{A.2}$$

where the subscripts on ψ denote the iteration count. Using the notation introduced in Eqs. (16), (18), and (19) this is determined as

$$\frac{\mathrm{d}\psi}{\mathrm{d}\sigma_{\mathrm{h}}} = 1 + \mathscr{K}\dot{\bar{\varepsilon}}\bar{\lambda}\frac{9}{8}q_1 q_2^2 \cosh\left(\frac{3q_2\sigma_{\mathrm{h}}}{2\bar{\sigma}}\right)\frac{1}{\bar{\sigma}}\left(\frac{a+b}{b+c}\right)^2\frac{c\,\Delta t}{1-(f-f_n)}, \tag{A.3}$$

where $\mathscr{K}$ is the elastic bulk modulus determined from

$$\mathscr{K} = -\mathscr{P}'\overline{V}\frac{1-(f-f_n)}{1-f_0}. \tag{A.4}$$

Appendix B

With the substitution of second term of Eq. (14) into Eq. (1), the yield function becomes

$$\phi = \left(\frac{\sigma_{\mathrm{e}}^T}{\bar{\sigma} + 3\mu\dot{\bar{\varepsilon}}\bar{\lambda}\Delta t}\right)^2 + 2q_1 f^* \cosh\left(\frac{3q_2\sigma_{\mathrm{h}}}{2\bar{\sigma}}\right) - \left(1 + q_1^2 f^{*2}\right), \tag{B.1}$$

where f^* and σ_{h} are implicit functions of $\dot{\bar{\varepsilon}}\bar{\lambda}$ through Eq. (23) and $\bar{\sigma}$ depends on $\dot{\bar{\varepsilon}} = \dot{\bar{\varepsilon}}\bar{\lambda}/\bar{\lambda}_t$.

A Newton–Rhapson iteration algorithm applied to Eq. (B.1) would determine corrections to $\dot{\bar{\varepsilon}}\bar{\lambda}$ as

$$\phi_{n+1} \simeq 0 = \phi_n + \frac{\mathrm{d}\phi}{\mathrm{d}\dot{\bar{\varepsilon}}\bar{\lambda}}\,\delta\left(\dot{\bar{\varepsilon}}\bar{\lambda}\right), \tag{B.2}$$

where the quantities are reevaluated for each iteration. Linearization of Eq. (B.1) with respect to $\dot{\bar{\varepsilon}}\bar{\lambda}$ gives

$$\begin{aligned}\frac{\mathrm{d}\phi}{\mathrm{d}(\bar{\lambda}\dot{\bar{\varepsilon}})} = & -2\left(\frac{\sigma_{\mathrm{e}}^{T}}{\bar{\sigma}+3\mu\dot{\bar{\varepsilon}}\bar{\lambda}\Delta t}\right)^{3}\left(\frac{\partial\bar{\sigma}}{\partial\dot{\varepsilon}}\frac{1}{\bar{\lambda}}+3\mu\Delta t\right)\frac{1}{\sigma_{\mathrm{e}}^{T}} \\ & +2\left[q_1\cosh\left(\frac{3q_2\sigma_{\mathrm{h}}}{2\bar{\sigma}}\right)-q_1^2 f^{*}\right]\frac{\mathrm{d}f^{*}}{\mathrm{d}f}\left(\frac{\mathrm{d}f}{\mathrm{d}\dot{\bar{\varepsilon}}\bar{\lambda}}+\frac{1}{\bar{\lambda}}\dot{f}_{\mathrm{N}\varepsilon}\Delta t+\dot{f}_{\mathrm{N}\sigma}\frac{\mathrm{d}\sigma_{\mathrm{h}}}{\mathrm{d}\dot{\bar{\varepsilon}}\bar{\lambda}}\right) \\ & +3q_1q_2 f^{*}\sinh\left(\frac{3q_2\sigma_{\mathrm{h}}}{2\bar{\sigma}}\right)\frac{1}{\bar{\sigma}}\left(\frac{\mathrm{d}\sigma_{\mathrm{h}}}{\mathrm{d}\dot{\bar{\varepsilon}}\bar{\lambda}}-\frac{\sigma_{\mathrm{h}}}{\bar{\sigma}}\frac{\partial\bar{\sigma}}{\partial\dot{\varepsilon}}\frac{1}{\bar{\lambda}}\right).\end{aligned} \tag{B.3}$$

The derivatives involving f and σ_{h} are

$$\frac{\mathrm{d}\sigma_{\mathrm{h}}}{\mathrm{d}\dot{\bar{\varepsilon}}\bar{\lambda}} = -\mathscr{K}\left(\frac{a+b}{b+c}\right)^{2}\frac{c\,\Delta t}{1-(f-f_n)}\left[Z-\dot{\bar{\varepsilon}}\bar{\lambda}\frac{9}{8}q_1q_2^{2}\cosh\left(\frac{3q_2\sigma_{\mathrm{h}}}{2\bar{\sigma}}\right)\frac{\sigma_{\mathrm{h}}}{\bar{\sigma}^{2}}\frac{\mathrm{d}\bar{\sigma}}{\mathrm{d}\dot{\bar{\varepsilon}}\bar{\lambda}}\right]\Big/\frac{\mathrm{d}\psi}{\mathrm{d}\sigma_{\mathrm{h}}}, \tag{B.4}$$

$$\frac{\mathrm{d}f}{\mathrm{d}\dot{\bar{\varepsilon}}\bar{\lambda}} = \left(\frac{a+b}{b+c}\right)^{2}c\,\Delta t\left[Z+\dot{\bar{\varepsilon}}\bar{\lambda}\frac{9}{8}q_1q_2^{2}\cosh\left(\frac{3q_2\sigma_{\mathrm{h}}}{2\bar{\sigma}}\right)\frac{1}{\bar{\sigma}}\left(\frac{\mathrm{d}\sigma_{\mathrm{h}}}{\mathrm{d}\dot{\bar{\varepsilon}}\bar{\lambda}}-\frac{\sigma_{\mathrm{h}}}{\bar{\sigma}}\frac{\mathrm{d}\bar{\sigma}}{\mathrm{d}\dot{\bar{\varepsilon}}\bar{\lambda}}\right)\right]. \tag{B.5}$$

where $\mathscr{K}$ is the bulk modulus, Eq. (A.4), and $\mathrm{d}\psi/\mathrm{d}\sigma_{\mathrm{h}}$ is given by Eq. (A.3).

Appendix C

Linearization of Eq. (26) to produce a stress increment as a function of the strain increment gives

$$\begin{aligned}\frac{\mathrm{d}\Delta\boldsymbol{\sigma}}{\mathrm{d}\Delta\boldsymbol{\varepsilon}} = & \left[\frac{1}{\lambda}\frac{\partial\bar{\sigma}}{\partial\dot{\bar{\varepsilon}}}-\frac{\bar{\sigma}}{\bar{\sigma}+3\mu\dot{\bar{\varepsilon}}\bar{\lambda}\Delta t}\left(\frac{1}{\lambda}\frac{\partial\bar{\sigma}}{\partial\dot{\bar{\varepsilon}}}+3\mu\Delta t\right)\right]\frac{\boldsymbol{\sigma}^{T}}{\bar{\sigma}+3\mu\dot{\bar{\varepsilon}}\bar{\lambda}3\mu\Delta t}\frac{\mathrm{d}\bar{\lambda}\dot{\bar{\varepsilon}}}{\mathrm{d}\Delta\boldsymbol{\varepsilon}} \\ & +\frac{\bar{\sigma}}{\bar{\sigma}+3\mu\dot{\bar{\varepsilon}}\bar{\lambda}\Delta t}\frac{\mathrm{d}\boldsymbol{\sigma}^{T}}{\mathrm{d}\Delta\boldsymbol{\varepsilon}}+\frac{\mathrm{d}\sigma_{\mathrm{h}}}{\mathrm{d}\bar{\lambda}\dot{\bar{\varepsilon}}}\mathbf{I}\otimes\frac{\mathrm{d}\bar{\lambda}\dot{\bar{\varepsilon}}}{\mathrm{d}\Delta\boldsymbol{\varepsilon}}+\frac{\mathrm{d}\sigma_{\mathrm{h}}}{\mathrm{d}\Delta\varepsilon_{V}}\mathbf{I}\otimes\frac{\mathrm{d}\Delta\varepsilon_{V}}{\mathrm{d}\Delta\boldsymbol{\varepsilon}},\end{aligned} \tag{C.1}$$

where the volumetric strain is identified as $\varepsilon_V = \ln(\overline{V})$. The derivatives of the hydrostatic stress appearing in the last two terms of Eq. (C.1) are determined in the iterative solution for the hydrostatic stress, Appendix A, and are given by

$$\frac{\mathrm{d}\sigma_{\mathrm{h}}}{\mathrm{d}\Delta\varepsilon_{V}} = \frac{\mathscr{K}}{(\mathrm{d}\psi/\mathrm{d}\sigma_{\mathrm{h}})} \tag{C.2}$$

and

$$\frac{\mathrm{d}f}{\mathrm{d}\Delta\varepsilon_{V}} = \frac{\mathrm{d}\sigma_{\mathrm{h}}}{\mathrm{d}\Delta\varepsilon_{V}}\left(\frac{a+b}{b+c}\right)^{2}c\,\Delta t\dot{\bar{\varepsilon}}\bar{\lambda}\frac{9}{4}q_1q_2^{2}\cosh\left(\frac{3q_2\sigma_{\mathrm{h}}}{2\bar{\sigma}}\right)\frac{1}{\bar{\sigma}}. \tag{C.3}$$

Two of the derivatives with respect to the strain increment are readily evaluated as

$$\frac{\mathrm{d}\boldsymbol{\sigma}^{T}}{\mathrm{d}\Delta\boldsymbol{\varepsilon}} = 2\mu\left(\mathscr{I}-\frac{1}{3}\mathbf{I}\otimes\mathbf{I}\right)\equiv 2\mu\mathscr{I}' \quad\text{and}\quad \frac{\mathrm{d}\Delta\varepsilon_{V}}{\mathrm{d}\Delta\boldsymbol{\varepsilon}} = \mathbf{I}. \tag{C.4}$$

The factor that remains to be defined is the derivative of $\bar{\lambda}\dot{\bar{\varepsilon}}$ with respect to the applied strain increment. This is determined from a linearization of the yield condition assuming that it a function of both the applied strain increment and the effective plastic strain rate. The particular form of the yield function used is introduced in Eq. (B.1).

$$\left.\frac{\mathrm{d}\phi}{\mathrm{d}\bar{\dot{\lambda}}\bar{\dot{\varepsilon}}}\right|_{\Delta\varepsilon}\frac{\mathrm{d}\bar{\dot{\lambda}}\bar{\dot{\varepsilon}}}{\mathrm{d}\Delta\boldsymbol{\varepsilon}}+\left.\frac{\mathrm{d}\phi}{\mathrm{d}\Delta\boldsymbol{\varepsilon}}\right|_{\bar{\dot{\lambda}}\bar{\dot{\varepsilon}}}=0. \tag{C.5}$$

The first factor in the first term was also needed in the iterative solution of the yield function. It is given by Eq. (B.3). With Eq. (B.1) chosen as the form of the yield function the second term can be computed as

$$\left.\frac{\partial\phi}{\mathrm{d}\Delta\boldsymbol{\varepsilon}}\right|_{\bar{\dot{\lambda}}\bar{\dot{\varepsilon}}}=\frac{\partial\phi}{\partial\sigma_{\mathrm{e}}^{T}}\frac{\mathrm{d}\sigma_{\mathrm{e}}^{T}}{\mathrm{d}\Delta\boldsymbol{\varepsilon}}+\left[\frac{\partial\phi}{\partial f^{*}}\frac{\partial f^{*}}{\partial f}\left(\frac{\mathrm{d}f}{\mathrm{d}\Delta\varepsilon_{V}}+\dot{f}_{N\sigma}\frac{\mathrm{d}\sigma_{\mathrm{h}}}{\mathrm{d}\Delta\varepsilon_{V}}\right)+\frac{\partial\phi}{\partial\sigma_{\mathrm{h}}}\frac{\mathrm{d}\sigma_{\mathrm{h}}}{\mathrm{d}\Delta\varepsilon_{V}}\right]\frac{\mathrm{d}\Delta\varepsilon_{V}}{\mathrm{d}\Delta\boldsymbol{\varepsilon}}, \tag{C.6}$$

where

$$\frac{\mathrm{d}\sigma_{\mathrm{e}}^{T}}{\mathrm{d}\Delta\boldsymbol{\varepsilon}}=3\mu\frac{\boldsymbol{\sigma}^{T}}{\sigma_{\mathrm{e}}^{T}} \tag{C.7}$$

and other derivatives are given by Eqs. (C.2)–(C.4). With the components of Eq. (C.6) known, Eq. (C.5) can be rearranged to give the final derivative need to evaluate Eq. (C.1).

$$\frac{\mathrm{d}\bar{\dot{\lambda}}\bar{\dot{\varepsilon}}}{\mathrm{d}\Delta\boldsymbol{\varepsilon}}=-\left.\frac{\mathrm{d}\phi}{\mathrm{d}\Delta\boldsymbol{\varepsilon}}\right|_{\bar{\dot{\lambda}}\bar{\dot{\varepsilon}}}\Big/\left.\frac{\mathrm{d}\phi}{\mathrm{d}\bar{\dot{\lambda}}\bar{\dot{\varepsilon}}}\right|_{\Delta\varepsilon}. \tag{C.8}$$

After considerable manipulation of the equations given above and using Eq. (13), the tangent stiffness becomes

$$\frac{\mathrm{d}\Delta\boldsymbol{\sigma}}{\mathrm{d}\Delta\boldsymbol{\varepsilon}}=A\mathscr{I}'+B\left(\frac{\boldsymbol{\sigma}'}{\bar{\sigma}}\otimes\frac{\boldsymbol{\sigma}'}{\bar{\sigma}}\right)+C\left(\frac{\boldsymbol{\sigma}'}{\bar{\sigma}}\otimes\mathbf{I}\right)+D\left(\mathbf{I}\otimes\frac{\boldsymbol{\sigma}'}{\bar{\sigma}}\right)+E(\mathbf{I}\otimes\mathbf{I}). \tag{C.9}$$

$$\begin{aligned}
A&=2\mu\left[1-\frac{3\mu\dot{\bar{\varepsilon}}\bar{\lambda}\Delta t}{\bar{\sigma}+3\mu\dot{\bar{\varepsilon}}\bar{\lambda}\Delta t}\right],\\
B&=2(3\mu)^{2}\Delta t\left[\frac{1}{\frac{1}{\lambda}\frac{\partial\bar{\sigma}}{\partial\bar{\varepsilon}}+3\mu\Delta t}-\frac{\dot{\bar{\varepsilon}}\bar{\lambda}}{\bar{\sigma}+3\mu\dot{\bar{\varepsilon}}\bar{\lambda}\Delta t}\right]\frac{\frac{1}{\lambda}\frac{\partial\bar{\sigma}}{\partial\bar{\varepsilon}}+3\mu\Delta t}{\bar{\sigma}+3\mu\dot{\bar{\varepsilon}}\bar{\lambda}\Delta t}\left(\frac{\mathrm{d}\phi}{\mathrm{d}\bar{\dot{\lambda}}\bar{\dot{\varepsilon}}}\right)^{-1},\\
C&=3\mu\Delta t\left[\frac{1}{\frac{1}{\lambda}\frac{\partial\bar{\sigma}}{\partial\bar{\varepsilon}}+3\mu\Delta t}-\frac{\dot{\bar{\varepsilon}}\bar{\lambda}}{\bar{\sigma}+3\mu\dot{\bar{\varepsilon}}\bar{\lambda}\Delta t}\right]\left(\frac{1}{\lambda}\frac{\partial\bar{\sigma}}{\partial\dot{\bar{\varepsilon}}}+3\mu\Delta t\right)\\
&\qquad\left[\frac{\partial\phi}{\partial f^{*}}\frac{\partial f^{*}}{\partial f}\left(\frac{\mathrm{d}f}{\mathrm{d}\Delta\varepsilon_{V}}+\dot{f}_{N\sigma}\frac{\mathrm{d}\sigma_{\mathrm{h}}}{\mathrm{d}\Delta\varepsilon_{V}}\right)+\frac{\partial\phi}{\partial\sigma_{\mathrm{h}}}\frac{\mathrm{d}\sigma_{\mathrm{h}}}{\mathrm{d}\Delta\varepsilon_{V}}\right]\left(\frac{\mathrm{d}\phi}{\mathrm{d}\bar{\dot{\lambda}}\bar{\dot{\varepsilon}}}\right)^{-1}\\
D&=-6\mu\frac{1}{\bar{\sigma}+3\mu\dot{\bar{\varepsilon}}\bar{\lambda}\Delta t}\frac{\mathrm{d}\sigma_{\mathrm{h}}}{\mathrm{d}\dot{\bar{\varepsilon}}\bar{\lambda}}\left(\frac{\mathrm{d}\phi}{\mathrm{d}\bar{\dot{\lambda}}\bar{\dot{\varepsilon}}}\right)^{-1},\\
E&=\frac{\mathrm{d}\sigma_{\mathrm{h}}}{\mathrm{d}\Delta\varepsilon_{V}}-\frac{\mathrm{d}\sigma_{\mathrm{h}}}{\mathrm{d}\dot{\bar{\varepsilon}}\bar{\lambda}}\left[\frac{\partial\phi}{\partial f^{*}}\frac{\partial f^{*}}{\partial f}\left(\frac{\mathrm{d}f}{\mathrm{d}\Delta\varepsilon_{V}}+\dot{f}_{N\sigma}\frac{\mathrm{d}\sigma_{\mathrm{h}}}{\mathrm{d}\Delta\varepsilon_{V}}\right)+\frac{\partial\phi}{\partial\sigma_{\mathrm{h}}}\frac{\mathrm{d}\sigma_{\mathrm{h}}}{\mathrm{d}\Delta\varepsilon_{V}}\right]\left(\frac{\mathrm{d}\phi}{\mathrm{d}\bar{\dot{\lambda}}\bar{\dot{\varepsilon}}}\right)^{-1}.
\end{aligned} \tag{C.10}$$

References

Aravas, N., 1987. On the numerical integration of a class of pressure-dependent plasticity models. International Journal of Numerical Methods in Engineering 24, 1395–1416.

Becker, R., 1987. The effect of porosity distribution on ductile failure. Journal for the Mechanics and Physics of Solids 35, 577–599.

Becker, R., Needleman, A., Richmond, O., Tvergaard, V., 1988. Void growth and failure in notched bars. Journal for the Mechanics and Physics of Solids 36, 317–351.

Brown, L.M., Embury, J.D., 1973. The initiation and growth of voids at second phase particles. In: The Microstructure and Design of Alloys, Proceedings of the Third International Conference on the Strength of Metals and Alloys, vol. 1. Institute of Metals, London, pp. 164–169.

Cady, C.M., Gray III, G.T., Hecker, S.S., Thoma, D.J., Korzekwa, D.R., Patterson, R.A., Dunn, P.S., Bingert, J.F., 1998. The plastic flow characteristics of uranium–niobium alloys as a function of strain rate and temperature. In: Khan, A.S. (Ed.), Constitutive and Damage Modeling of Inelastic Deformation and Phase Transformation. Neat Press, Maryland, USA, pp. 15–18.

Chu, C.C., Needleman, A., 1980. Void Nucleation effects in biaxially stretched sheets. Journal of Engineering Materials and technology 102, 249–256.

Drucker, D.C., 1959. A definition of stable inelastic material. Journal of Applied Mechanics 26; Transactions of the American Society of Mechanical Engineers 81, 101–106.

Drucker, D.C., 1960. Plasticity. In: Goodier, J.N., Hoff, N.J. (Eds.), Structural Mechanics, Proceedings of the First Symposium on Naval Structural Mechanics. Pergamon Press, New York, pp. 407–447.

Drucker, D.C., Li, M., 1993. Triaxial test instability of a nonassociated flow-rule model. Journal of Engineering Mechanics 119, 1188–1204.

Dube, E., Neely, R., Nichols, A., Sharp, R., Couch, R., 2001. Users Manual for ALE3D—An arbitrary Lagrange/Eulerian 3D Code System. Lawrence Livermore National Laboratory.

Gourdin, W.H., Weinland, S.L., Boling, R.M., 1989. Development of the electromagnetically launched expanding ring as a high-strain-rate test technique. Review of Scientific Instrumentation 60, 427–432.

Grady, D.E., Benson, D.A., 1983. Fragmentation of metal rings by electromagnetic loading. Experimental Mechanics 23, 393–400.

Gurson, A.L., 1977. Continuum theory of ductile rupture by void nucleation and Growth: part I-yield criteria and flow rules for porous ductile media. Journal of Engineering Materials and Technology 99, 2–15.

Han, J.-B., Tvergaard, V., 1995. Effects of inertia on the necking behavior of ring specimens under rapid radial expansion. European Journal of Mechanics A/Solids 14, 287–307.

Hill, R., Hutchinson, J.W., 1975. Bifurcation phenomena in the plane tension test. Journal of the Mechanics and Physics of Solids 23, 239–264.

Hutchinson, J.W., Neale, K.W., 1978. Sheet necking-III. Strain-rate effects. In: Koistinen, D.P., Wang, N.-M. (Eds.), Mechanics of Sheet Metal Forming. Plenum Publishing Co., New York, pp. 269–285.

Johnson, J.N., Addessio, F.L., 1988. Tensile Plasticity and ductile fracture. Journal of Applied Physics 64, 6699–6712.

Kailasam, M., Aravas, N., Ponte Castañeda, P., 2000. Porous metals with developing anisotropy: constitutive models, computational issues and applications to deformation processing. Computer Modeling in Engineering & Sciences 1, 105–118.

Koplik, J., Needleman, A., 1988. Void growth and coalescence in porous plastic solids. International Journal of Solids and Structures 24, 835–853.

Krieg, R.D., Krieg, D.B., 1977. Accuracies of numerical solutions methods for the elastic-perfectly plastic model. Journal of Pressure Vessel Technology 99, 510–515.

Leblond, J.-B., Perrin, G., Devaux, J., 1995. An improved Gurson-type model for hardenable ductile metals. European Journal of Mechanics A/Solids 14, 499–527.

Liu, C., Huang, Y., Stout, M.G. On the application of Gurson's theory to voided solids with rate sensitive matrices, submitted for publication.

Mahnken, R., 1999. Aspects on the finite-element implementation of the Gurson model including parameter identification. International Journal of Plasticity 15, 1111–1137.

Mott, H.F., 1947. Fragmentation of shell cases. Proceedings of the Royal Society of London 300, 300–308.

Needleman, A., Tvergaard, V., 1984. Limits to formability in rate-sensitive metal sheets. In: Carlsson, J., Ohlson, N.G. (Eds.), Mechanical Behaviour of Materials-IV. Pergamon Press, New York, pp. 51–65.

Niordson, F.I., 1965. A unit for testing materials at high strain rates. Experimental Mechanics 5, 29–32.

Olsen, M.L., Sunwoo, A., Ring, R.R., Chambers, R.M., in preparation.

Pandolfi, A., Krysl, P., Ortiz, M., 1999. Finite element simulation of ring expansion and fragmentation: the capturing of length and time scales through cohesive models of fracture. International Journal of Fracture 95, 279–297.

Pardoen, T., Doghri, I., Delannay, F., 1998. Experimental and numerical comparison of void growth models and void coalescence criteria for the prediction of ductile fracture in copper bars. Acta Materialia 46, 541–552.

Pardoen, T., Hutchinson, J.W., 2000. An extended model for void growth and coalescence. Journal for the Mechanics and Physics of Solids 48, 2467–2512.

Press, W.H., Teukolsky, S.A., Vetterling, W.T., Flannery, B.P., 1992. Numerical Recipes in FORTRAN: The Art of Scientific Computing. Cambridge University Press, Cambridge, p. 359.

Rice, J.R., 1976. The localization of plastic deformation. In: Koiter, W.T. (Ed.), Proceedings of the 14th International Congress on Theoretical and Applied Mechanics. North-Holland Publishing Co., Amsterdam, pp. 207–220.

Saje, M., Pan, J., Needleman, A., 1982. Void nucleation effects on shear localization in porous plastic solids. International Journal of Fracture 19, 163–182.

Sørensen, N.J., Freund, L.B., 2000. Unstable neck formation in a ductile ring subjected to impulsive radial loading. International Journal of Solids and Structures 37, 2265–2283.

Sunwoo, A.J., Hiromoto, D.S., Chan, J.W. Effects of natural aging on tensile properties of as-formed U–6%Nb alloy, submitted for publication.

Thomason, P.F., 1999. Ductile spallation fracture and the mechanics of void growth and coalescence under shock-loading conditions. Acta Materialia 43, 3633–3646.

Tvergaard, V., 1981. Influence of voids on shear band instabilities under plane strain conditions. International Journal of Fracture 17, 389–407.

Tvergaard, V., Needleman, A., 1984. An analysis of the cup-cone fracture in a round tensile bar. Acta Metallurgica 32, 157–167.

Yamamoto, H., 1978. Conditions for shear localization in the ductile fracture of void containing materials. International Journal of Fracture 14, 347–365.